* Manuscript

Controlled Support MEG Imaging

Srikantan Nagarajan[1*], Oleg Portniaguine[2],

Dosik Hwang[2], Chris Johnson[2] and Kensuke Sekihara[3]

[1]Biomagnetic Imaging Laboratory, Department of Radiology, University of California at San Francisco, San Francisco, CA 94122, USA

[2]Scientific Computing and Imaging Institute, School of Computing, University of Utah, Salt Lake City, UT 84108

[3]Department of Electronic Systems and Engineering,Tokyo Metropolitan Institute of Technology, Asahigaoka 6-6, Hino, Tokyo 191-0065, Japan, USA

* Corresponding author: sri@radiology.ucsf.edu

Abstract

In this paper, we present a novel approach to imaging of sparse and focal neural current sources from MEG (magnetoencephalography) data. Using the framework of Tikhonov regularization theory, we introduce a new stabilizer that uses the concept of *controlled support* to incorporate *a priori* assumptions about the area occupied by the focal sources. The paper discusses the underlying Tikhonov theory and its relationship to a Bayesian formulation which in turn allows us to interpret and better understand other related algorithms.

I. Introduction

The brain's neuronal activity generates weak magnetic fields (10 fT- 1 pT). Magnetoenchephalography (MEG) is an non-invasive technique for characterizing these magnetic fields using an array of superconducting quantum interference devices (SQUIDS). SQUID magnetometers can measure the changes in the brain's magnetic field on a millisecond timescale, thus, providing unique insights into the dynamic aspects of the brain's activity. The goal of biomagnetic imaging is to use MEG data to characterize macroscopic dynamic neural information by solving an electromagnetic source localization problem.

In the past decade, the development of source localization algorithms has significantly progressed [1]. Currently, there are two general approaches to estimating MEG sources: parametric methods and tomographic imaging methods [2]. With parametric methods, a few current dipoles of uknown location and moment represent the sources. In this case, the inverse problem is a non-linear optimization in which one estimates the position and magnitude of the dipoles.

In this paper, we use the tomographic imaging method, where a grid of small voxels represents entire brain volume. The inverse problem then seeks to recover a whole brain activation image, represented by the moments and magnitudes of elementary dipolar sources located at each voxel. The advantage of such a formulation is that the forward problem becomes linear. However, the ill-posed nature of the imaging problem constitutes considerable difficulty, most notably due to the non-uniqueness of the solution.

A common way to constrain the non-uniqueness is to use the weighted minimum norm methods. Such methods find solutions that match the data while minimizing a weighted l_2 norm of the solution [2] [3] [4], [5]. Unfortunately, these techniques tend to "smear" focal sources over the entire reconstruction region.

There are three basic approaches for creating less smeared solutions to the MEG focal imaging problem: 1) use of l_p norms, 2) Bayesian estimation procedures with sparse priors, and 3) iterative reweighting methods. The first approach that produces sparse solutions uses an l_1, or an l_p norm. Although, the l_1 norm solution can be formulated as a linear programming problem which converges to the global solution, other l_p norm methods are calculated

using multidimensional iterative methods which often do not converge to the correct solution. Furthermore, all l_p methods are sensitive to noise [6] [7]. The second approach that performs better than the first one, is a Bayesian framework with sparse priors derived from Gibbs distributions [8]. However, these methods are very computationally intensive since full *a posteriori* estimation is solved using the Markov-chain Monte-Carlo or mean-field approximation methods [9], [10], [11]. The third approach is iterative reweighted minimum norm method. The method uses a weighting matrix which, as the iterations proceed, reinforces strong sources and reduces weak ones [12] [13]. The problems associated with this method are sensitivity to noise, high dependency on the initial estimate and tendency to accentuate the peaks of the previous iteration. In addition, the method often produces an image of a focal source as a scatterred cloud of multiple sources that exist near each other.

In this paper, we combine features of all three approaches outlined above and derive a novel Controlled Support MEG imaging algorithm, using Tikhonov regularization theory. The advantages of our algorithm are the quality of focal source images as well as robustness and speed. In Section II of this paper, we formulate the MEG inverse problem under the framework of Tikhonov regularization theory, and introduce a way to constrain the problem using specially selected stabilizing functionals. We then describe the relationship of this formulation to the minimum-norm methods and Bayesian methods. In Section III, we revisit minimum support stabilizing functional which obtains the sparsest possible solutions, but may produce an image of a focal source as a cloud of points. To remedy this problem, in Section IV we derive a new Controlled Support functional, by adding an extra constraining term to the Minimum Support functional. In Section V, we will explain details of computationally efficient method of reweighted optimization. Section VI explains how the numerical minimization is carried out. In Section VI, we demonstate performance of the algorithm using results from Monte-Carlo simulation studies with realistic sensor geometries and variety of noise levels.

II. Formulation of the MEG inverse problem using Tikhonov regularization

Let the three Cartesian coordinates of the current dipole strength for each one of the

$N_s/3$ voxels be denoted by the length N_s vector $\mathbf{s}$.. The data consists of a vector $\mathbf{b}$ that contains magnetic field measurements at all receivers. The length of the $\mathbf{b}$ is determined by the number of sensor sites, as denoted by N_b. The forward modeling operator $\mathbf{L}$ connects the model to the data:

$$\mathbf{Ls} = \mathbf{b}, \tag{1}$$

where $\mathbf{L}$ is also known as the "lead field." The lead field is a matrix of size $N_b \times N_s$ that connects the spatial distribution of the dipoles $\mathbf{s}$ to measurements at the sensors $\mathbf{b}$. According to Hadamard [14], the three difficulties in an inverse problem are: 1) the solution of the inverse problem may not exist, 2) the solution may be non-unique, 3) the solution may be unstable. The Tikhonov regularization theory resolves these difficulties using the notions of misfit, the stabilizer and the Tikhonov parametric functional.

The notion of misfit minimization resolves the first difficulty, the non-existence of the solution. In the event that an exact solution does not exist, we search for the solution that fits the data approximately, using the misfit functional as a goodness-of-fit measure. Following the tradition [15], we use a quadratic form of the misfit functional, denoted as ϕ:

$$\phi(\mathbf{s}) = \|\mathbf{Ls} - \mathbf{b}\|^2 / \|\mathbf{b}\|^2. \tag{2}$$

When the model produces a misfit that is smaller than the noise level, (Tikhonov discrepancy principle), this model could be a solution of the problem.

The second difficulty, the non-uniqueness, is a situation where many different models have misfits smaller than the noise level. All of these models could be solutions of the problem. In practice, we need only one solution that is good. The stabilizing functional, denoted $S(\mathbf{s})$, measures goodness of the solution. Designing the stabilizer S is a difficult task which we will discuss in detail in the next two sections. In simplest terms, S is small for "good" models and large for "bad" models. Therefore, the weighted sum of misfit and stabilizer (denoted as P) measures both the goodness of data fit and goodness of the model:

$$P(\mathbf{s}) = \phi(\mathbf{s}) + \lambda S(\mathbf{s}), \tag{3}$$

where λ is regularization parameter and P is Tikhonov parametric functional. Both difficulties considered so far, (non-uniqueness and non-existence), are resolved by posing the

minimization of parametric functional:

$$\mathbf{s} = argmin_{\mathbf{s}} P(\mathbf{s}) \tag{4}$$

The third difficulty, the ill-conditioning, is a situation where small variation in the data results in large variation in the solution. Careful choice of regularization parameter λ resolves this difficulty. In short, the Tikhonov discrepancy principle defines the choice of λ, which is discussed in Section III.

In summary, the formulation of MEG inverse problem using Tikhonov regularization reduces to minimization of the Tikhonov parametric functional (4).

Finally, we note that a probabilistic framework provides a similar view on the inverse problem [16]. A Bayesian approach poses the *Maximum a posteriori* (MAP) problem:

$$\mathbf{s} = argmax_{\mathbf{s}} \left(\exp\left(-(\mathbf{Ls} - \mathbf{b})^T (\mathbf{Ls} - \mathbf{b}) \right) \cdot \exp\left(-\lambda S(\mathbf{s}) \right) \right). \tag{5}$$

Note that the logarithm of (5) is (4). While using different underlying axioms, the Tikhonov problem results in a formulation similar to the Bayesian approach. In the Bayesian framework, the functional $\exp\left(-\lambda S(\mathbf{s})\right)$ incorporates prior assumptions on distribution of $\mathbf{s}$. A stabilizer function in the Tikhonov framework can be viewed as the log of the prior probability drawn from an expontential distributions on the sources, without the normalization terms for probability distributions. For example, a quadratic functional would correspond to a Gaussian prior, an linear functional corresponds to a Laplacian prior and a P-norm functional would correspond to a sparse distribution drawn from the exponential family.

III. The minimum support stabilizer

As discussed in the previous section, the role of a stabilizer is especially important for a situation in which many different models produce similar data. Clearly, the misfit functional alone cannot discriminate between these models. Therefore, this situation requires using additional discriminatory measure, such as the stabilizing functional.

The choice of the stabilizing functional S is difficult. S should be small for good models and large for bad models, so that the minimum of S determines the solution. Unfortunately,

the definition of a good model relies upon empiricial knowledge and depends upon each particular problem.

The good model for MEG inverse problem should adequately represent focal current sources, *i.e.*, sources that occupy a small volume (or, sources with small support). Therefore, the minimum support functional [17] [18], (denoted as S_{min}), is one possible choice for the stabilizer:

$$S_{min}(\mathbf{s}) = \frac{1}{N_s} \sum_{1}^{N_s} \frac{s_k^2}{s_k^2 + \beta^2} \tag{6}$$

where s_k is a component of vector $\mathbf{s}$.

To better understand physical meaning of the minimum support stabilizer consider the following form of S_{min}:

$$S_{min}(\mathbf{s}) = \frac{1}{N_s} \|sign(\mathbf{s})\|^2, \tag{7}$$

where *sign* denotes signature function

$$sign(x) = \begin{bmatrix} 1, & if & x > 0 \\ 0, & if & x = 0 \\ -1, & if & x < 0 \end{bmatrix} \tag{8}$$

Continuous approximation of the $sign^2$ function is better for numerical implementation:

$$sign(s_k)^2 = \frac{s_k^2}{s_k^2 + \beta^2} \quad , \quad \beta^2 = 10^{-16} \cdot max(\mathbf{s})^2, \tag{9}$$

where constant 10^{-16} is machine precision. Note that, substituting (9) into (7) leads to (6). The form (7) is convenient to understand the physical meaning of S_{min}. Functional S_{min} measures a fraction of non-zero parameters. In other words, S_{min} measures support. If we use S_{min} as a stabilizer, we define the good model as one with the small support.

However, not all images with small support are suitable for imaging of focal MEG sources. As indicated in Figure 1, sometimes the minimum support method represents a single focal source as a cloud of scattered points which can be misinterpreted as multiple local sources located near each other (panel a). What we ideally want in this situation is an image of a single patch, as depicted in panel (b) of Figure 1. We note that this problem has also been reported by the researchers working with other types of sparse priors [11]. In the next

section, we deal with this problem by introducing additional restrictive term to the minimum support stabilizer.

IV. Controlled support stabilizer

The controlled support stabilizer (denoted as S_{con}) is a functional that reaches its minimum for images with a predetermined support value α. That value should be small, but not so small that it creates the undesirable of producing scatterred sources. In other words, the image in Figure 1 case b, which we consider to be good, produces a minimum of the stabilizer S_{con}. The undesirable (scattered) image (case a in the same Figure) corresponds to a larger value of stabilizer S_{con}. This discriminative effect of S_{con} happens because S_{con} is a weighted sum of the previously introduced minimum support stabilizer S_{min} and an additional restricting term S_{reg}:

$$S_{con}(\mathbf{s}) = (1-\alpha) \ \cdot \ S_{min}(\mathbf{s}) + \alpha \ \cdot \ S_{reg}(\mathbf{s}), \tag{10}$$

where the restricting term S_{reg} is:

$$S_{reg}(\mathbf{s}) = \frac{1}{max|\mathbf{s}| \sum_{k=1}^{N_s} |s_k|} \sum_{k=1}^{N_s} s_k^2 = \frac{\|\mathbf{s}\|_{l_2}^2}{\|\mathbf{s}\|_{l_\infty} \|\mathbf{s}\|_{l_1}}. \tag{11}$$

Upon examining expression (11) we notice that the functional S_{reg} has opposing properties to S_{min}, S_{reg} has a maximum where S_{min} has a minimum. Obviously, the choice of the weighting factor α determines the balance between terms $(1-\alpha)S_{min}$ and αS_{reg}. In summary, S_{min} favors minimum support solutions, S_{reg} favors solutions with large support, and S_{con} favors solutions with support controlled by the value of α.

The remainder of this section addresses two important details. First, we must explain why the effect of S_{reg} is opposite to that of S_{min}. Second, we will discuss the normalizations of S_{min} and S_{reg}, which leads to their invariance to discretization. We must note that S_{reg} is the square of the l_2 norm weighted by the product of l_∞ and l_1 norms (11). We think of S_{reg} as a normalized l_2 norm. Therefore, the minimum of S_{reg} is reached at the minimum l_2 norm solution (a solution with large support where S_{min} has maximum). The maximum of S_{min} is 1, which happens for a case with one non-zero parameter, where S_{con} is at its minimum.

Strictly speaking, the maximum of S_{reg} is also possible for other cases. However, opposing properties of the minimums are more important for our purposes.

Now, we consider the normalizations of S_{min} and S_{reg}. Factor $1/N_s$ normalizes S_{min} (6), while divisions by l_1 and l_∞ norms normalize stabilizer S_{reg} (11). Normalizations are important for the meaningful summation of S_{min} and S_{reg} in expression (10), because they make the terms bounded:

$$0 \leq S_{min} \leq 1 \quad 0 \leq S_{reg} \leq 1. \tag{12}$$

In addition, normalizations make functionals S_{min} and S_{reg} invariant to discretization and grayscale of the image. To illustrate this property, consider an example 2-D image with a total of 100 pixels, where 96 pixels are zero, and a compact domain in the middle contains 4 pixels – all with the value of a. The left panel in Figure 2 illustrates this case. The following calculations find values of S_{min} and S_{reg} for this case:

$$\begin{gathered} N_s = 100, \;\; \textstyle\sum_{k=1}^{N_s} abs(s_k) = 4a, \;\; \max(\mathbf{s}) = a, \\ \\ \textstyle\sum_{k=1}^{N_s} sign(s_k)^2 = 4, \;\; \textstyle\sum_{k=1}^{N_s} s_k^2 = 4a^2, \\ \\ S_{min} = \textstyle\sum_{k=1}^{N_s} sign(s_k)^2/100 = 0.04 \\ \\ S_{reg} = \textstyle\sum_{k=1}^{N_s} (s_k)^2 / \left(\sum_{k=1}^{N_s} abs(s_k) \cdot max(\mathbf{s}) \right) = \frac{4a^2}{4a \cdot a} = 1 \end{gathered} \tag{13}$$

According to (13), $S_{min} = 0.04$ (which is a fraction of the non-zero pixels in the image from Figure 2) and $S_{reg} = 1$. Now, we refine the discretization twice. The resulting image has total of 400 pixels with 16 pixels containing the value of a, as shown in the right panel of Figure 2. Calculations similar to (13) show that S_{min} and S_{reg} did not change ($S_{min} = 0.04$ and $S_{reg} = 1$). This example also shows that functional values are invariant to a (image level, or grayscale). Note that the same properties hold true for 3-D grids and volume models that we consider in this paper.

V. The method of reweighted optimization

In this section, we discuss how to solve minimization problem using the method of reweighted optimization. To obtain the final form of the objective functional (denoted as P_{con}), we substitute definitions (2) (6) (10) (11) into (3):

$$P_{con} = \frac{\|\mathbf{Ls}-\mathbf{b}\|^2}{\|\mathbf{b}\|^2} + \lambda\left(\frac{1-\alpha}{N_s}\sum_{k=1}^{N_s}\frac{s_k^2}{s_k^2+\beta^2} + \frac{\alpha}{\|\mathbf{s}\|_{l_\infty}\cdot\|\mathbf{s}\|_{l_1}}\sum_{k=1}^{N_s}s_k^2\right). \tag{14}$$

In this section, we discuss the idea of how to solve the minimization problem:

$$\mathbf{s} = argmin_{\mathbf{s}} P_{con}(\mathbf{s}). \tag{15}$$

Arguably, the minimization of P_{con} is difficult, because it is a non-linear (non-quadratic) functional of $\mathbf{s}$. We have two feasible options for the numerical solution of our non-quadratic problem. The first uses gradient-type inversion methods, and the second uses the method of reweighted optimization. While the gradient-type minimization method is well known [19], this method requires computing the gradient of a functional (14). Computing such a gradient is problematic since we previously used *sign* while constructing P_{con} (see formulas (8) and (9)).

In this paper, we use the method of reweighted optimization, a historical choice for related minimum-support problem [17], [18], [20]. In addition, a number of researchers have found the reweighted optimization convenient [21] [22], [23], especially for cases where non-linearity is represented by weights to the quadratic term. This is exactly our case. Notice that the term s_k^2 in (14) can be taken out of the brackets

$$P_{con} = \frac{\|\mathbf{Ls}-\mathbf{b}\|^2}{\|\mathbf{b}\|^2} + \lambda\sum_{k=1}^{N_s}\left(\frac{1-\alpha}{N_s}\frac{1}{s_k^2+\beta^2} + \frac{\alpha}{\|\mathbf{s}\|_{l_\infty}\cdot\|\mathbf{s}\|_{l_1}}\right)s_k^2. \tag{16}$$

Thus, model-dependent weighting of the quadratic functional represents the non-linearity in (14):

$$P_{con} = \frac{\|\mathbf{Ls}-\mathbf{b}\|^2}{\|\mathbf{b}\|} + \lambda\sum_{k=1}^{N_s} w_k^{-2}\cdot s_k^2, \tag{17}$$

where w_k is model-dependent weight

$$w_k^{-2} = \frac{1-\alpha}{N_s}\frac{1}{s_k^2+\beta^2} + \frac{\alpha}{\|\mathbf{s}\|_{l_\infty}\cdot\|\mathbf{s}\|_{l_1}}. \tag{18}$$

It is convenient to assemble weights into a sparse diagonal matrix $\mathbf{W}(\mathbf{s})$ with terms w_k in the main diagonal, and write (17) in matrix notations:

$$P_{con} = \frac{\|\mathbf{Ls} - \mathbf{b}\|^2}{\|\mathbf{b}\|^2} + \lambda\|\mathbf{W}(\mathbf{s})^{-1}\mathbf{s}\|^2 \tag{19}$$

To understand our optimization algorithm in detail, it is necessary to convert the parametric functional to a purely quadratic form, which has a known analytic solution. This form is obtained by transforming the problem into a space of weighted model parameters. To do that, we insert $\mathbf{W}(\mathbf{s})\mathbf{W}(\mathbf{s})^{-1}$ term into (19):

$$P_{con} = \frac{\|\mathbf{LW}(\mathbf{s})\mathbf{W}(\mathbf{s})^{-1}\mathbf{s} - \mathbf{b}\|^2}{\|\mathbf{b}\|^2} + \lambda\|\mathbf{W}(\mathbf{s})^{-1}\mathbf{s}\|^2. \tag{20}$$

Then, we transform (20) by replacing the variables:

$$\mathbf{s} = \mathbf{W}(\mathbf{s})\mathbf{s}_w,\ \mathbf{L}_w = \mathbf{LW}(\mathbf{s}). \tag{21}$$

After substituting (21), expression (20) results in a purely quadratic form of the functional with respect to $\mathbf{s}_w$:

$$P(\mathbf{s}_w) = \frac{\|\mathbf{L}_w\mathbf{s}_w - \mathbf{b}\|^2}{\|\mathbf{b}\|^2} + \lambda\|\mathbf{s}_w\|^2. \tag{22}$$

Since $P_{con}(\mathbf{s}_w)$ is purely quadratic with respect to $\mathbf{s}_w$, the minimization problem for $P_{con}(\mathbf{s}_w)$ has an analytical solution, known as the Riesz representation theorem [24]:

$$\mathbf{s}_w = \mathbf{L}_w^T(\mathbf{L}_w\mathbf{L}_w^T + \lambda\|\mathbf{b}\|^2\mathbf{I}_b)^{-1}\mathbf{b}, \tag{23}$$

where $\mathbf{I}_b$ is unit matrix in the space of data (of size $N_b \times N_b$).

Thus, the idea of reweighted optimization is to solve (15) iteratively, assuming the weights are constant on each iteration. Starting from the initial guess for the weights, we can use the Riesz representation theorem to find weighted solution. We can then convert back to original space, update the weights depending on the solution, and repeat the iterative process. The next section discusses the details of this process. The above equation is identical to the MAP estimator with Gaussian priors for the sources and the noise, where the source variance is assumed to be an unknown diagonal matrix and the noise variance is known and parameterized by λ.

VI. The minimization algorithm

The algorithm for minimizing a parametric functional is iterative. On each iteration, (enumerated with index n), we compute the updates of: the weights $\mathbf{W}_n$, the weighted lead fields $\mathbf{L}_{\mathbf{w}n}$, the weighted model $\mathbf{s}_{\mathbf{w}n}$, and the update of the model $\mathbf{s}_n$. These quantities depend upon values from previous iteration (denoted with index $n-1$). Inputs to the algorithm include the data $\mathbf{b}$, noise level estimate ϕ_0, as well as the support parameter α. Before the first iteration, we precompute the lead fields $\mathbf{L}$, set weights to one $\mathbf{W}_0 = \mathbf{I}_s$, and set the current model update to zero $\mathbf{s}_0 = 0$. The important additional step are incorporated in the final algorithm. The first is the choice of regularization parameter, the second is the line search correction, and the third is termination criterion.

According to Tikhonov condition, the choice of the regularization parameter λ should be such that the misfit (2) at the solution equals an *a priori* known noise level ϕ_0 [25],:

$$\frac{\|\mathbf{L}_w\mathbf{s}_w - \mathbf{b}\|^2}{\|\mathbf{b}\|^2} = \phi_0. \tag{24}$$

Substituting (23) into (24) yields the equation

$$\|\mathbf{L}_{\mathbf{w}n}\mathbf{L}_{\mathbf{w}n}^T(\mathbf{L}_{\mathbf{w}n}\mathbf{L}_{\mathbf{w}n}^T + \lambda\|\mathbf{b}\|\mathbf{I}_\mathbf{b})^{-1}\mathbf{b} - \mathbf{b}\|^2 = \phi_0\|\mathbf{b}\|^2 \tag{25}$$

which we solve with a fixed point iteration method. In equation (25) the only unknown variable is the scalar parameter λ. Since the Gramm matrix $\mathbf{L}_{\mathbf{w}n}\mathbf{L}_{\mathbf{w}n}^T$ is small ($N_b \times N_b$, where N_b is small), the fixed point iteration method easily solves equation (25) for λ. For the cases where the data dimension N_b is large, which makes the direct inversion of a Gramm matrix impractical, solving equation (22) using the Riesz theorem (23) can be substituted by solving (22) via a conjugate gradient method [20]. In this paper, we consider processing of MEG data from an array of 102 sensors, so the dimension of data is small $N_b = 102$ and therefore the Gramm matrix is easily invertible with direct methods. Such a choice of the regularization term is analagous to setting the noise variance in the Bayesian MAP estimation procedure.

Second, to ensure convergence of the algorithm, we incorporate a line search procedure. Convergence of the reweighted optimization depends upon how accurately the equation (22)

approximates the original non-quadratic equation (19). That, in turn, depends on assumption of constant weights, which, in our case, are dependent on $\mathbf{s}$. The usual assumption for any iterative method is that the changes in a model are small from one iteration $\mathbf{s}_{n-1}$ to the next $\mathbf{s}_n$. That assumption may not always hold, and therefore, steps which converge on equation (22) may be divergent on the original equation (16) due to significant changes in $\mathbf{W}(\mathbf{s})$. The well known method of line search [19] serves to correct this problem. Once the next approximate update $\mathbf{s}'_n$ is found from the previous update $\mathbf{s}_{n-1}$ using the approximate formula (22), we check the value of original non-linear objective functional $P_{con}(\mathbf{s}'_n)$. If the objective functional decreases, the line search is not deployed. If the objective functional increases, (which signifies the divergent step), we perform a line search.

If $P_{con}(\mathbf{s}_{n-1}) < P_{con}(\mathbf{s}_n)$, we perform a line search, by searching for the minimum of P_{con} with respect to the scalar variable t (the step length):

$$t = argmin_t P_{con}(\mathbf{s}_{n-1} + t(\mathbf{s}'_n - \mathbf{s}n - 1))$$

If $P_{con}(\mathbf{s}_{n-1}) > P_{con}(\mathbf{s}_n)$, then we set $t = 1$ and do not perform the line search. Note that the smaller step size t is, the closer the corrected update $\mathbf{s}_n$ is to the previous update $\mathbf{s}_{n-1}$ from which the weights $\mathbf{W}_n$ were derived. Thus, the smaller t is the less weights change from $n-1$ iteration to n, and therefore, our quadratic approximation becomes more accurate. With small enough t, a smaller value of P_{con} will always be found somewhere between $\mathbf{s}_{n-1}$ and $\mathbf{s}'_n$. Minimization of the scalar functional P_{con} with respect to scalar argument t is a simple 1-D problem. That problem is solved by sampling the function at a few points (usually three or four), fitting the parabola into it, and finding the argument of a minimum. Such sampling is fast, for one estimate of the functional we only need to solve one forward problem. In many previously conducted studies with minimum support functional S_{min}, the reweighted optimization has never diverged [17] [18]. Our new controlled support functional, S_{con}, is dominated by term S_{min}. Therefore, we expected the same good convergence for S as was reported for S_{min}. However, in the Monte-Carlo simulations carried out in this paper and with some limited datasets, the algorithm has never called the line search routine because the divergence was never detected.

Third, the termination criterion was formulated based on the following two observations.

First, we must observe that all updates $\mathbf{s}_n$ produce the same misfit ϕ_0 (due to enforcement of the Tikhonov condition). Therefore, only the second term S_{con} determines the minimum of $P_{con}(\mathbf{s}_n)$ on a given set of arguments $\mathbf{s}_n$. This second term consists of two parts: $(1-\alpha)S_{min}(\mathbf{s}_n)$, and $\alpha S_{reg}(\mathbf{s}_n)$. The second observation is that the $S_{min}(\mathbf{s}_n)$ term decreases with n, and the $S_{reg}(\mathbf{s}_n)$ term increases with n. This happens because on the first iteration $n=1$ we produce the minimum norm solution, and then progress towards more focused solutions (see discussion about opposing properties of S_{min} and S_{reg} in section III). So, the dominance of αS_{reg} term over $(1-\alpha)S_{min}$ term signifies close proximity to the minimum of P_{con}.

We summarize the complete algorithm as follows:

1. Compute $\mathbf{L}_{\mathbf{w}n}$ using (21)

$$\mathbf{L}_{\mathbf{w}n} = \mathbf{L}\mathbf{W}_{n-1}.$$

2. Determine regularization parameter by fixed point iteration of equation (25).
3. Find the weighted model $\mathbf{s}_{\mathbf{w}n}$ using (23):

$$\mathbf{s}_{\mathbf{w}n} = \mathbf{L}_{\mathbf{w}n}^T(\mathbf{L}_{\mathbf{w}n}\mathbf{L}_{\mathbf{w}n}^T + \lambda\|\mathbf{b}\|\mathbf{I}_{\mathbf{b}})^{-1}\mathbf{b}.$$

4. Find preliminary update of the model $\mathbf{s}_n$ using (21),

$$\mathbf{s}'_n = \mathbf{W}_{n-1}\mathbf{s}_{\mathbf{w}n}.$$

5. Check for divergence and incorporate line search.
6. Corrected update $\mathbf{s}_n$ is found from the previous update $\mathbf{s}_{n-1}$ using step length t:

$$\mathbf{s}_n = \mathbf{s}_{n-1} + l(\mathbf{s}'_n - \mathbf{s}_{n-1}).$$

7. Check for termination criterion. We stop iterations if

$$(1-\alpha)S_{min}(\mathbf{s}_n) < \alpha S_{reg}(\mathbf{s}_n).$$

8. Find the updated weight $\mathbf{W}_n$ using (18). and go to Step 1, repeating all steps in the loop.

VII. Results and Discussion

In simulations we demonstrate the algorithm performance, estimate localization accuracy and speed of the method. The geometry for all simulations were from an MR (Magnetic Resonance) image of a subject. Figure 3 shows a head surface extracted from the MR volume image. We transformed the MEG sensor array to MRI coordinates by matching the reference points (measured on the subject's head) and the extracted head surface [26]. Figure 3 shows the MEG array as a "helmet" consisting of 102 square sensor "plates." Each plate has magnetic coils that measure the normal (to the plate) component of the magnetic field. The middle of the plate serves as a reference point. In order to parameterize the inverse problem, we divided the volume of the brain into 30,000 cubic voxels of size $4 \times 4 \times 4$ millimeters. Vector $\mathbf{s}$ consists of strengths of three components of current dipoles within each voxel. This produces $N_s = 90,000$ free inversion parameters (unknowns). This parameterization takes into account both gray matter and white brain matter. We did not use the alternative parameterization with the cortical surface constraint because the final reconstruction result would strongly depend on the accuracy of the cortical surface extraction procedure. The controlled support algorithm is the point of our investigation. So, we did not use cortical surface extraction since it may mask the evaluation of the algorithm's performance.

We built the underlying forward model (lead field operator) using the formula for a dipole in a homogeneous sphere [3] We computed the sensitivity kernel for each sensor (a row of matrix $\mathbf{L}$), using an individual sphere locally fit to the surface of the head near that particular sensor site [27].

As a first numerical experiment, we placed two dipoles within the brain, approximately at the level of the primary auditory cortex. Figure 4 shows the location of dipoles within the brain. That setup defines the vector $\mathbf{s}$ as zeros everywhere except the specified dipole locations. We generate the data $\mathbf{b}$ using the forward equation (1), adding Gaussian random noise such that the SNR is 400. The level of noise is set relative to the data and measured in the same units as a normalized misfit, as defined by the formula

$$\mathbf{b}_{noise} = \mathbf{b} + \mathbf{n}\frac{\|\mathbf{b}\|}{\|\mathbf{n}\| \cdot SNR} \tag{26}$$

where SNR is the signal-to-noise ratio defined by the ratio of the average signal power across channels divided by the average noise power, and $\mathbf{n}$ is the noise vector. Figure 5 shows the

resulting data as a flat projection.

To illustrate convergence, Figure 6 shows the evolution of stabilizers during iterations, and Figure 7 shows the evolution of the solution. The isolines in Figure 7 display the magnitudes of the dipoles in the solutions, superimposed on a corresponding MRI slice.

Figure 7 displays six solutions produced on each iteration. The first solution (Panel 1) is a minimum norm solution that is smooth, and maximums are far away from the true dipole locations. In contrast to a common misconception about reweighted optimization methods, observe how the location of maximum activation shifts during reweighted iterations (Panels 1-6 in Figure 7). Note that the method discussed here does not simply accentuate the peaks of the previous iteration. The size and shape of the estimated source area are mainly due to the model and the noise level and do not directly relate to the size and shape of the orignal source.

Each of these solutions describe the data equally well, but they do not describe the prior expectations that the activity is focused. The solutions are indistinguishable in terms of the data fit, however, they have different values of the stabilizer. Figure 6 shows evolutions of a stabilizer S (solid line) and its individual components $(\alpha-1)S_{min}$ (dots) and αS_{reg} (dashes). We see that the first solution has a large value of a stabilizer, and on the next iterations, the stabilizer decreases to a minimum.

We have empirically determined, from our Monte-Carlo experiments, that the best estimate of the dipole location is not the maximum of the image, but rather the location of the maximum of a local weighted average of the image around its maximum solution. Such a technique is better since it provides estimates located away from the grid nodes, and is, therefore, less sensitive to a given inversion grid. We estimate the dipole locations by thresholding the whole image at 10% to the maximum, separating the individual maximums by clustering, and determining the center of each cluster as the average of a position of cluster points with weights corresponding to the intensity of the image. This procedure is very fast for our compact images (fractions of a second) and does not increase the overall computation time.

Second, we estimate the localization accuracy and speed of our algorithm using the Monte-

Carlo study with 100 simulations. Each experiment is a separate round of inversion run on a data generated by a dipole with a random orientation and a random location within the brain. Figure 8 shows a histogram of the root-mean-square localization error. The mean error was 2.1 mm, the three largest errors were 8,10 and 12 mm, all for dipoles located very deep within the brain or at the corners of the mesh. Four errors were below 8 mm, and the rest of 93 errors were below 4 mm. These results are consistent with performance reported in the literature for single-dipole parametric inversion [28]. With the geometrical setup described above, and using a 700 MHz PC, the localization runs for 30 seconds.

Third, we run the source localization with different levels of noise, ranging from small (SNR=400) to high (SNR=4). Table 1 summarizes the results. Each column in the table is averaged from 100 Monte-Carlo trials. Expectedly, under high levels of noise localization accuracy as well as errors in orientation deteriorates. However, the method performed robustly and converged well even under 25 % of noise and even in this case exhibited localization accuracy of 10 mm.

Table.1 Results from Monte-Carlo simulation study

$Error \setminus Noise$	400	100	67	33	16	8	4
$Location[mm]$	2.55	2.76	3.80	4.36	6.43	8.58	10.90
$Orientation[degree]$	1.35	1.50	1.94	2.62	4.13	4.78	6.18

Acknowledgements

This work was partially supported under NIH grant P41 RR12553-03 and also by grants from the Whitaker Foundation and NIH (R01DC004855) to SN. The authors would like to thank Dr. M. Funke from the University of Utah Department of Radiology for his help providing the realistic MEG array geometry and Blythe Nobleman from Scientific Computing and Imaging Institute at the University of Utah, for her many useful suggestions pertaining to the manuscript.

References

[1] S. Baillet, J.C. Mosher, and R.M. Leahy. Mapping human brain function using intrinsic electromagnetic signals. *IEEE Signal Processing Magazine, in press*, 2001.

[2] M. Hamalainen, R. Hari, R.J. Ilmoniemi, J. Knuutila, and O.V. Lounasmaa. Magnetoencephalography - theory, instrumentation, and applications to noninvasive studies of the working braing. *Reviews in Modern Physics*, 65:413–497, 1993.

[3] J. Sarvas. Basic mathematical and electromagnetic concepts of the biomagnetic inverse problem. *Phys. Med. Biol.*, 32:11–22, 1987.

[4] J.Z. Wang, S. J. Williamson, and L. Kaufman. Magnetic source images determined by a lead-field analysis: the unique minimum-norm least-squares estimation. *IEEE Trans Biomed Eng*, 39(7):665–675, 1992.

[5] R. D. Pascual-Marqui and R. Biscay-Lirio. Spatial resolution of neuronal generators based on eeg and meg measurements. *Int J Neurosci*, 68(1-2):93–105, 1993.

[6] K. Matsuura and Y. Okabe. Selective minimum-norm solution of the biomagnetic inverse problem. *IEEE Trans Biomed Eng*, 42(6):608–615, 1995.

[7] K. Uutela, M. Hamalainen, and E. Somersalo. Visualization of magnetoencephalographic data using minimum current estimates. *Neuroimage*, 10(2):173–180, 1999.

[8] D.M. Schmidt, J.S. George, and C.C. Wood. Bayesian inference applied to the electromagnetic inverse problem. *Hum Brain Mapp*, 7(3):195–212, 1999.

[9] C. Bertrand, Y. Hamada, and H. Kado. Mri prior computation and parallel tempering algorithm: a probabilistic resolution of the meg/eeg inverse problem. *Brain Topogr*, 14(1):57–68, 2001.

[10] C. Bertrand, M. Ohmi, R. Suzuki, and H. Kado. A probabilistic solution to the meg inverse problem via mcmc methods: the reversible jump and parallel tempering algorithms. *IEEE Trans Biomed Eng*, 48(5):533–542, 2001.

[11] J.W. Phillips, R. M. Leahy, and J. C. Mosher. Meg-based imaging of focal neuronal current sources. *IEEE Trans Med Imaging*, 16(3):338–348, 1997.

[12] I.F. Gorodnitsky and B.D. Rao. Sparse signal reconstruction from limited data using focuss: A recursive weighted norm minimumization algorithm. *IEEE Trans. on Signal Processing*, 45:600–616, 1997.

[13] I.F. Gorodnitsky and J.S. George. Neuromagnetic source imaging with focuss: a recursive weighted minimum norm algorithm. *Electroencephalogr Clin Neurophysiol*, 95(4):231–51, 1995.

[14] J. Hadamard. Sur les problemes aux derivees parielies et leur signification physique. *Bull. Univ. of Princeton*, pages 49–52, 1902. in French.

[15] U. Eckhart. Weber's problem and weiszfeld's algorithm in general spaces. *Math. Programming*, 18:186–196, 1980.

[16] S. Baillet and L. Garnero. A bayesian approach to introducing anatomo-functional priors in the eeg/meg inverse problem. *IEEE Trans Biomed Eng*, 44(5):374–385, 1997.

[17] B.J. Last and K. Kubik. Compact gravity inversion. *Geophysics*, 48:713–721, 1983.

[18] O. Portniaguine and M.S. Zhdanov. Focusing geophysical inversion images. *Geophysics*, 64:874–887, 1999.

[19] R. Fletcher. *Practical methods of optimization*. Wiley and Sons, 1981.

[20] O. Portniaguine. *Image focusing and data compression in the solution of geophysical inverse problems*. PhD thesis, University of Utah, 1999.

[21] R. Wolke and H. Schwetlick. Iteratively reweighted least squares: algorithms, convergence analysis, and numerical comparisons. *SIAM, J. Sci.Stat. Comput.*, 9:907–921, 1988.

[22] D.P. O'Leary. Robust regression computation using iteratively reweighted least squares. *SIAM J. Matrix Anal. Appl.*, 11:466–480, 1990.

[23] C. G. Farquharson and D.W. Oldenburg. Non-linear inversion using general measures of data misfit and model structure. *Geophysical Journal International*, 134:213–227, 1998.

[24] C.D. Aliprantis and O. Burkinshaw. *Locally solid Riesz spaces*. Academic Press, New York & London, 1978.

[25] A.N. Tikhonov and Y.V. Arsenin. *Solution of ill-posed problems*. Winston and Sons, 1977.

[26] D. Kozinska, F. Carducci, and K. Nowinski. Automatic alignment of eeg/meg and mri data sets. *Clinical Neurophysiology*, 112:1553–1561, 2001.

[27] M.X. Huang, J.C. Mosher, and R.M. Leahy. A sensor-weighted overlapping-sphere head model and exhaustive head model comparison for meg. *Phys Med Biol*, 44(2):423–440, 1999.

[28] R.M. Leahy, J.C. Mosher, M.E. Spencer, M.X. Huang, and J.D. Lewine. A study of dipole localization accuracy for meg and eeg using a human skull phantom. *Electroencephalogr Clin Neurophysiol*, 107(2):159–173, 1998.

Figures

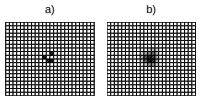

Fig. 1. This Figure illustrates outcomes of two attempts to image a single focal source with two different stabilizers. a) Image obtained with minimum support stabilizer is a cloud of disconnected multiple focal sources located near each other. b) Image obtained with controlled support stabilizer is a single patch.

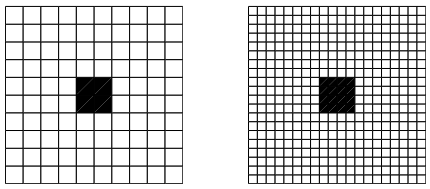

Fig. 2. Functionals S_{min} and S_{reg} are invariant to image level and discretization. For illustration, consider a 2-D model depicted in this Figure. Model has a non-zero domain in the middle. Left panel, shows case with 100 pixels and 4 non-zeros. Functional values for this model are $S_{min} = 0.04$ and $S_{reg} = 1$. Right panel, same case with finer discretization, 400 pixels and 16 non-zero values.

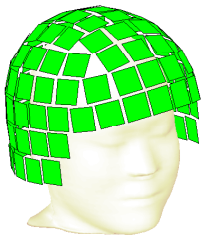

Fig. 3. Geometry that was used in the model study. An outer head surface was extracted from the subject's MRI. MEG sensor array (a "hat" consisting of square receiver "plates", as shown here) was positioned in MRI coordinates by matching the reference points to the head surface. Each "plate" measures normal component of a magnetic field.

Fig. 4. Location of two test dipoles (stars) within the head.

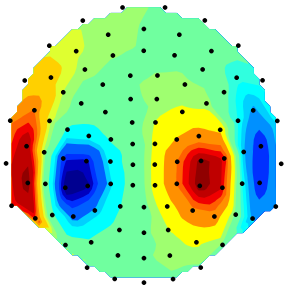

Fig. 5. Magnetic field data for two-dipole model (the model from Figure 4). Data are shown by color map superimposed on flat projection of measuring array (the helmet from Figure 3). Dots show the locations of the sensors, each sensor corresponds to one plate in Figure 3. Data contain Gaussian random noise such that the SNR=400.

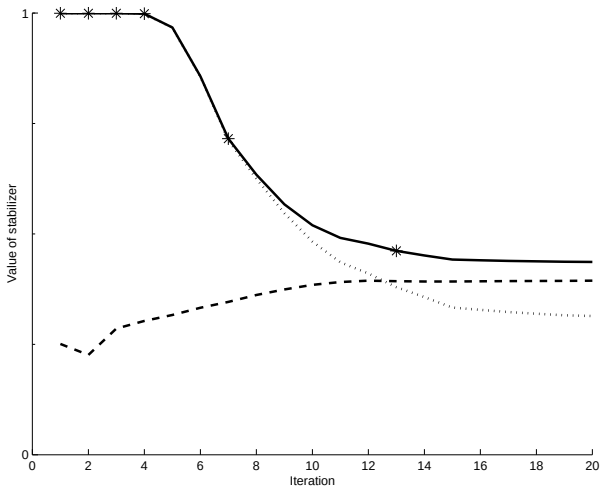

Fig. 6. Evolution of stabilizers during reweighted iterations. Solid line shows evolution of S, dashes show evolution of αS_{reg} and dots show the evolution of $(1-\alpha)S_{min}$. Stars show the stopping point, where term $(1-\alpha)S_{min}$ becomes less than term αS_{reg}. After that point term αS_{reg} (dashes) dominates, and S_{con} (solid line) flattens, as illustrated by this Figure.

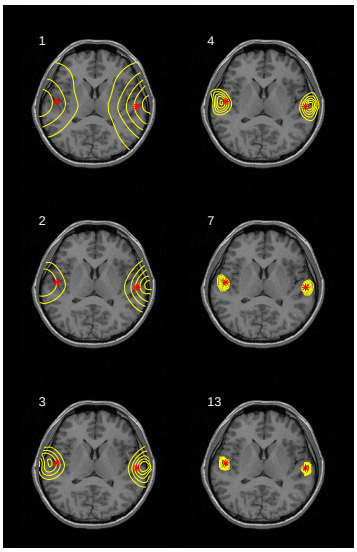

Fig. 7. Evolution of solution during reweighted iterations. The case corresponds to example discussed in Figure 6. Stars show "true" location of dipoles (location of dipoles within the head is shown in Figure 4). Solution is superimposed on corresponding MRI slice as isolines. Panels numbered 1,2,3,4,7,13 show the solutions at the corresponding iteration.

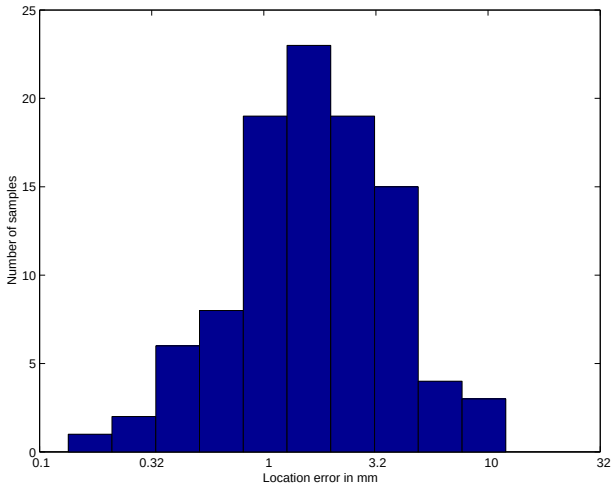

Fig. 8. Histogram of localization errors for 100 experiments with a randomly located dipole. Average error is 2.1 mm, seven errors are above 4 mm.